

Highlights

A novel numerical model of two-phase flow considering multiple bubble sizes in an alkaline water electrolyzer

Ryo Kanemoto, Takuto Araki, Shigenori Mitsushima

- Simulation of bubble flow in a water electrolyzer for several current densities.
- Multiple bubble size classes were considered within the framework of Euler-Euler model.
- Each size class has its own distinct velocity and volume fraction fields.
- Simulation results were compared to experimental visualization results.
- Importance of considering multiple size classes was demonstrated.

A novel numerical model of two-phase flow considering multiple bubble sizes in an alkaline water electrolyzer

Ryo Kanemoto^a, Takuto Araki^b, Shigenori Mitsushima^{c,d}

^a*Graduate School of Engineering Science, Yokohama National University, 79-5, Hodogaya, Yokohama, 2408501, Kanagawa, Japan*

^b*Faculty of Engineering, Division of Systems Research, Yokohama National University, 79-5, Hodogaya, Yokohama, 2408501, Kanagawa, Japan*

^c*Institute of Advanced Sciences, Yokohama National University, 79-5, Hodogaya, Yokohama, 2408501, Kanagawa, Japan*

^d*Green Hydrogen Research Center, Yokohama National University, 79-5, Hodogaya, Yokohama, 2408501, Kanagawa, Japan*

Abstract

Precise description of bubble flow behavior is vital to predict the performance of water electrolysis. This study employed the Euler-Euler model to simulate bubble flow within an alkaline water electrolysis cell. The dispersed gas bubble phase was categorized into three bubble size classes with the representative diameters of 30 (small), 90 (medium), and 270 μm (large), where velocity and volume fraction fields were calculated for each class. Simulations were conducted for three current densities and the results highlighted distinct flow field differences among the three size classes. This behavior can be attributed to the balance between viscous drag and buoyancy force, which scales with the specific surface area of the bubbles. The simulation results were compared with experimental visualization in terms of the descending height of bubble circulation along the liquid flow. Additional simulation with only the medium size class was compared to that with three size classes and the necessity of considering multiple size classes was confirmed.

Keywords:

Alkaline water electrolysis, CFD, Two-phase flow, Multiple dispersed phase

1. Introduction

Hydrogen, conventionally produced primarily through petroleum refining for various industrial applications, is now drawing attention for its production via water electrolysis due to the growing demand for it as a carrier of renewable energy. However, the proportion of hydrogen produced through water electrolysis remains relatively very low compared to overall production [1]. This should be addressed by drastically improving the energy efficiency of water electrolysis and lowering the hydrogen costs. There are three major types of water electrolysis: proton exchange membrane type, alkaline type, and solid oxide type. In order to produce hydrogen with renewable energy, which has a fluctuating and intermittent output, an ideal water electrolysis system must be able to start up in a short time and have a broad load flexibility range [2]. In terms of that, proton exchange membrane water electrolysis (PEMWE) seems to be the best option.

Nevertheless, the major type for large-scale hydrogen production is currently AWE since it offers low investment costs and relies on mature traditional technology. While PEMWE uses noble metals like platinum and iridium oxide as its electrocatalysts, AWE uses non-noble metals like nickel and iron, which makes the investment costs of AWE cheaper than those of PEMWE. Besides, the lifetime of AWE systems is longer and the annual maintenance costs are lower compared to PEMWE systems [3, 4]. However, AWE needs improvement in its dynamic performance. It is often mentioned that AWE has a long start-up time and a slow dynamic response to the variation of load. Therefore, the dynamic behavior of AWE must be deeply investigated to design and install much larger scales of hydrogen production systems. One of the important factors that affect the dynamic response is the presence of bubbles, which can modify the modality of heat and mass transport [5, 6]. Especially for the industrial

scale of AWE cells, since they are oftentimes long in the direction of gravity, the volume fraction of bubble in the vicinity of the electrodes can vary considerably depending on location, which makes the electrodes experience heterogeneity and can ultimately lead to electrode degradation. Therefore, we study the influence of the bubble-liquid flow on the dynamic behavior of the electrochemical performance, for which experimental and computational approaches are available. While experimental investigations play a crucial role in understanding the dynamic behavior [7], conducting experiments with industrial scale AWE cells often requires high cost. Hence, a macroscopic computational approach that models the behavior of an entire cell or stack can be also effective to obtain a comprehensive data about the physical properties of interest. A computational simulation of an AWE cell is a multiphysics that consists of two main parts: a fluid flow model to describe the mass transport of fluid and an electrochemical model. Here, in a macroscopic simulation, these two models have to be bridged by another model to consider the interaction between the electrochemical reactions at the electrode surface and the mass transport in the fluid part. However, since there is no such model that is well-established yet, our target in this paper is limited to the modelling of the bubble-liquid flow and its evaluation.

Bubble-liquid flow is modeled with two main methods: separated phase models and dispersed phase models [8]. The separated phase models, which include interface capturing method and interface tracking method, are useful when simulating the detailed surface motion of bubbles. However, for an industrial scale AWE cell, the separated phase models require huge computational cost, thus making the dispersed phase models more desirable. Among the several dispersed phase models, the Euler-Euler model is suitable to deal with a large number of particles and momentum exchanges between bubbles and liquid.

For the particle size of the dispersed phase, monodisperse size distribution is selected in some cases [9, 10, 11]. However, since the size variation of electrochemically generated bubbles is so large [12, 13, 14] that monodisperse models [11, 15, 16] are inadequate to deal with the difference in the behavior of different size bubbles, polydisperse models are more appropriate for the bubble-liquid flow inside a water electrolyzer. As a part of polydisperse models, population balance model (PBM) has been studied by many researchers and various types of

PBMs have been developed [17].

The basic concepts behind PBM is to consider the conservation of number density function by solving a population balance equation. Here, number density function represents the number distribution of dispersed particle size (usually volume or diameter). By extracting Sauter diameters from the number density function and use them in the Euler-Euler model CFD simulation, the detailed flow fields for different particle sizes can be estimated.

The existing studies of CFD simulations coupled with PBM have provided valid and accurate results in polydisperse systems. However, most of those studies deal only with bubble columns as their targets to apply PBM. While bubble column reactors sometimes even have a circulation flow by having components that induce a downward flow, to our best knowledge, no studies have applied PBM to bubble columns with circulation flow [18, 19, 20, 21]. In general, water electrolyzers have a circulation flow inside them, and since electrochemically generated bubbles have a wide range of size distribution, the velocity fields for each bubble size are often different from one another. Since PBM has only a single momentum equation for the entire dispersed phase, it is not easy to accurately simulate flow systems where there are significant variations in velocity fields depending on the different sizes of the dispersed phase.

Therefore, in this paper, we introduce a polydisperse model that holds multiple size classes, each of which has its own momentum equation so that the different velocity fields are simulated for different size classes. This feature allows for simulating flow fields with significant variations not only in the magnitude but also even in the direction of velocity fields for each particle size class. Using this model, we focused on simulating the bubble-liquid flow field in an alkaline water electrolysis cell.

2. Physical Setup

Fig.1 shows anode side of the alkaline water electrolysis cell used for validation of the presented CFD model. Note that we focus on the fluid flow field, which we do not consider; This cell is zero-gap mono-polar type and only its anode side is considered in the simulation, since this study's target is the fluid flow field. The potassium hydroxide solution (KOH) was pumped from the inlet at the bottom of the acrylic case and flows out from the outlet in the middle. Since this cell was primarily

designed to investigate local electrochemical behavior, the nickel expanded metal electrode is divided into two parts: the main electrode and a smaller electrode, although the latter was not used in this study. As electric current is applied, oxygen bubbles are generated from the main electrode. The measurements for validation were performed at the following three current densities: $j = 0.3, 0.6, 1.0$ [A/cm²].

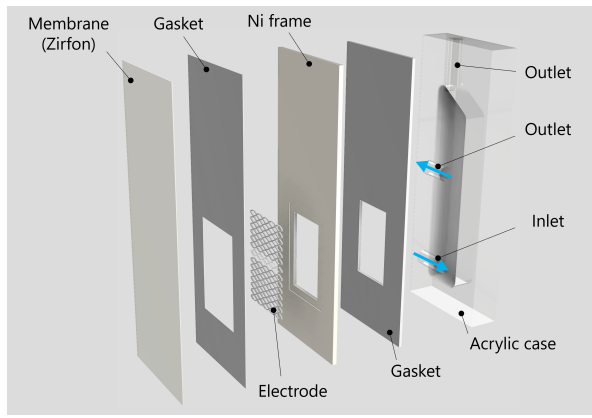


Figure 1: Configuration of the experimental AWE anodic half-cell, with electrolyte flow indicated by the blue arrows indicate. The smaller electrode is rendered as transparent since it was not in use. Some components are omitted for simplicity.

3. Governing equations

The simulation of bubble-liquid flow in an alkaline water electrolyzer in this work was performed using reactingMultiphaseEulerFoam, a multiphase flow solver in OpenFOAMv2006 based on the Eulerian model [22]. This solver can deal with multiple different fluid components to simulate a multiphase flow involving chemical reactions, and the velocity fields can be calculated for each different component. Although this study does not explicitly deal with chemical reactions, this feature can be exploited to calculate the velocity fields for the bubbles of each different size class by considering each bubble size group as a separate component. Thus, in the bubble-liquid flow simulation, when we introduce N classes of bubble size, all we consider are N gas phases and one liquid phase, i.e., a total of $N + 1$ phases. Each of the phases has its own phase fraction field, and they satisfy the following equation:

$$\sum_i^N \alpha_i + \alpha_l = 1, \quad (1)$$

where α is the phase volume fraction, and the subscripts i and l represent the bubble size class and the liquid phase, respectively. The continuity and momentum equations are written as:

$$\frac{\partial}{\partial t} (\alpha_i \rho_i) + \nabla \cdot (\alpha_i \rho_i \mathbf{u}_i) = \dot{m}_i, \quad (2)$$

$$\begin{aligned} \frac{\partial}{\partial t} (\alpha_i \rho_i \mathbf{u}_i) + \nabla \cdot (\alpha_i \rho_i \mathbf{u}_i \mathbf{u}_i) \\ = -\alpha_i \nabla p + \nabla \cdot (\alpha_i \tau_i) + \alpha_i \rho_i g + M_{il} \end{aligned} \quad (3)$$

for the bubble size class i , and

$$\frac{\partial}{\partial t} (\alpha_l \rho_l) + \nabla \cdot (\alpha_l \rho_l \mathbf{u}_l) = 0, \quad (4)$$

$$\begin{aligned} \frac{\partial}{\partial t} (\alpha_l \rho_l \mathbf{u}_l) + \nabla \cdot (\alpha_l \rho_l \mathbf{u}_l \mathbf{u}_l) \\ = -\alpha_l \nabla p + \nabla \cdot (\alpha_l \tau_l) + \alpha_l \rho_l g - M_{il} \end{aligned} \quad (5)$$

for the liquid phase l . Here, the momentum equation for the liquid phase is Reynolds averaged and the Reynolds stress is modeled by the standard $k-\varepsilon$ model. In these equations, ρ is phase density, \mathbf{u} is phase velocity vector, g is the gravitational acceleration, and \dot{m}_i is a volumetric mass source term that is only active in the computational cells facing the electrode boundary, which is explained in Section 4. Also, τ is the stress tensor, which is expressed as

$$\tau = \mu \left\{ 2\mathbf{D} - \frac{2}{3} \text{tr}(\mathbf{D}) \mathbf{I} \right\}, \quad (6)$$

where \mathbf{D} is the strain rate tensor described as

$$\mathbf{D} = \frac{1}{2} \left\{ \nabla \mathbf{u} + (\nabla \mathbf{u})^T \right\}. \quad (7)$$

The viscosity μ is defined as $\mu_i = \mu_g^{\text{mol}}$ for the gas phases and $\mu_l = \mu_l^{\text{mol}} + \mu_l^{\text{turb}}$ for the liquid phase, where μ^{mol} is the molecular dynamic viscosity of the phase, and μ^{turb} is the turbulent viscosity (or eddy viscosity). Since we used the standard $k-\varepsilon$ model, the turbulent viscosity is estimated as

$$\mu_l^{\text{turb}} = C_\mu \frac{\rho_l k^2}{\varepsilon}, \quad (8)$$

where k is turbulent kinetic energy and ε is turbulent energy dissipation rate.

We considered the momentum transfer between the bubble size class i and the liquid phase as M_{il} in each momentum transport equation, which is the summation of drag (F_D), virtual mass (F_{VM}), lift (F_L), wall lubrication (F_{WL}), turbulent dispersion (F_{TD}) forces:

$$M_{il} = F_D + F_{VM} + F_L + F_{WL} + F_{TD} \quad (9)$$

The drag force F_D results from the viscosity of the continuous phase when the dispersed phase has a slip-velocity against the continuous phase and it acts in the opposite direction of the slip-velocity.

$$F_D = -\frac{3}{4} \frac{C_D}{d_i} \alpha_i \rho_l |\mathbf{u}_i - \mathbf{u}_l| (\mathbf{u}_i - \mathbf{u}_l), \quad (10)$$

where $\mathbf{u}_i - \mathbf{u}_l$ represents the slip-velocity of the bubble class i against the liquid phase l , d_i is the diameter of the bubble class i , and C_D is the drag coefficient which is determined by Schiller and Naumann model [23]:

$$C_D = \begin{cases} \frac{24}{Re_b} (1 + 0.15 Re_b^{0.687}) & (Re_b \leq 1000) \\ 0.44 & (Re_b > 1000) \end{cases} \quad (11)$$

where Re_b is the Reynolds number of the bubble $Re_b = \rho_l |\mathbf{u}_i - \mathbf{u}_l| d_i / \mu_l$. The Schiller and Naumann model is applied to spherical particles. This study deals with the microscale bubbles, whose Eötvös number is sufficiently small that the bubbles can be considered spherical.

The virtual mass (or added mass) force F_{VM} is generated when the dispersed particles are accelerated relative to the continuous phase [24]. The relative acceleration of a particle results in carrying some volume of the surrounding fluid along with it, which in turn increases the effective inertia of the particle. The virtual mass force is expressed as:

$$F_{VM} = C_{VM} \alpha_i \rho_l \left(\frac{D\mathbf{u}_i}{Dt} - \frac{D\mathbf{u}_l}{Dt} \right), \quad (12)$$

where C_{VM} is the virtual mass coefficient, which is known to be 0.5 for a spherical particle.

The lift force F_L accounts for the transversal motion of the dispersed particles due to the velocity gradients in the continuous phase [25], which is expressed as:

$$F_L = C_L \alpha_i \rho_l (\mathbf{u}_i - \mathbf{u}_l) \times (\nabla \times \mathbf{u}_l), \quad (13)$$

where C_L is the lift coefficient, which is set to 0.5.

The wall lubrication force F_{WL} was incorporated to mitigate the overestimation of the gas volume fraction near the wall, where the velocity boundary layer exists around the bubbles. Without this force, the velocity gradients near the wall cause a dominance of the lift force, which makes the bubbles get overly pushed towards the wall. We adopted the wall lubrication model derived by Antal et al. [26], which is expressed as:

$$F_{WL} = \frac{C_{WL}}{d_i} \alpha_i \rho_l |(\mathbf{u}_i - \mathbf{u}_l)|^2 \mathbf{n}_w, \quad (14)$$

where $(\mathbf{u}_i - \mathbf{u}_l)$ is the bubble relative velocity component tangential to the wall, \mathbf{n}_w is the normal vector of the wall with the inward direction, and C_{WL} is the wall lubrication coefficient:

$$C_{WL} = \max \left(0, C_{w1} + C_{w2} \frac{d_i}{2y_w} \right), \quad (15)$$

where y_w is the distance to the nearest wall, and C_{w1} and C_{w2} are the constant coefficients with adopted values of -0.1 and 0.15, respectively.

The turbulent dispersion force F_{TD} was employed to include the influence of the turbulent random fluctuations on the redistribution of bubbles in the transversal direction [27]. We used the model derived by Burns [28], which is expressed as:

$$F_{TD} = -\frac{3}{4} \frac{C_D}{d_i} \alpha_i |\mathbf{u}_i - \mathbf{u}_l| \frac{\mu_l^{\text{turb}}}{Sc_{TD}} \left(\frac{1}{\alpha_i} + \frac{1}{1 - \alpha_i} \right) \nabla \alpha_i, \quad (16)$$

where Sc_{TD} is the Schmidt number of turbulent dispersion, which is set to 1.0.

Note that we assumed bubbles do not to break up or coalesce in the entire simulation domain. Firstly, the bubbles of interest in this paper are on the microscale and therefore not prone to breaking up easily. Secondly, coalescence does not occur frequently in the bulk, where the spacing between any bubble pairs is often ample [29, 30]. However, coalescence admittedly occurs in the vicinity of electrode or at the areas where bubbles accumulate, such as free liquid surface or ceilings. As for the vicinity of the electrode, the bubble diameters to be inputted to the simulation are those of bubbles that have already coalesced with other bubbles and detached from the electrode surface (see Section 5), so a particular coalescence model does not have to be used. Regarding the areas where bubbles accumulate, since they are densely populated with a high

frequency of coalescence events, it is better to have some coalescence model. Nevertheless, modelling bubble coalescence is not within the scope of this paper, so any coalescence is not considered.

4. Boundary conditions

The simulation geometry is shown in Fig. 2. The uniform velocity boundary condition is applied to very phase at the inlet boundary, which is $\mathbf{u}_i = (-0.032, 0, 0)$ [m/s]. At the outlet boundary, a constant pressure condition is applied. All the other boundaries including the top face of the geometry are set as no-slip wall boundaries. For every phase volume fraction field, zero-gradient condition is applied to all the boundaries.

The volumetric mass source for the bubble class i in Eq. 2 is defined as:

$$\dot{m}_i = c_i \frac{jM}{C_{\text{reac}} F}, \quad (17)$$

where j is the current density, M is the molar mass of the product chemical specie, C_{reac} is the number of electrons that is required to produce one molecule of the product chemical specie, and F is Faraday's constant. The fractional part composed of these quantities gives the total mass of the chemical species produced by the electrochemical reaction. To allocate this total mass to each bubble size class i , allocation coefficient c_i is multiplied. Accordingly, the sum of c_i must be equal to 1. Note that the mass of water vapor inside bubbles is negligible since the saturation vapor pressure is very low at the temperature of interest, which is 25 °C. In addition, we considered the bubbles' initial velocity at the electrode as zero.

Here, the outlet boundary is extended sufficiently further from the electrode because the pressure boundary at the outlet leads to reverse flow, which causes a violation of Eq. 1. In Fig. 2, however, the outlet is only displayed up to the necessary length.

5. Bubble size classes

In this study, three size classes X1, X2, and X3 were considered. The representative bubble diameter d_i for bubble size class $i = \text{X1, X2, or X3}$ and its allocation coefficient c_i were determined based on an experimental visualization. Fig. 3 shows a random frame from the visualized video. The video was

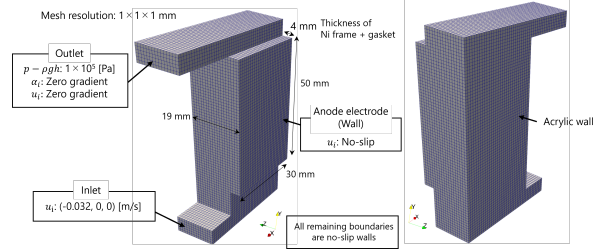


Figure 2: Simulation geometry of the anodic half-cell, where oxygen is produced, and the boundary conditions for main fields.

recorded at 6000 fps, 1024×1024 pixels, and shows the bottom 4 mm square of the electrode, giving a resolution of $3.9 \mu\text{m}/\text{pixel}$. In the video, a control surface with its normal vector parallel to the direction of gravity is set. The diameters of all bubbles passing through the control surface within a randomly selected 0.02 seconds were recorded. Three sets of this procedure (i.e., 0.06 seconds in total) were performed at each current density.

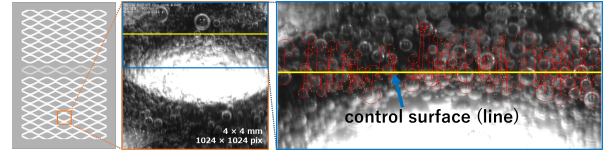


Figure 3: Measurement of bubble diameter from the experimental visualization.

To obtain the mass of each bubble, equation of state was considered:

$$P_{\text{in}} \frac{4}{3} \pi \left(\frac{d}{2} \right)^3 = \frac{m}{M} RT, \quad (18)$$

where P_{in} is the pressure inside the bubble, d is the bubble diameter measured in the experimental videos, m is the bubble mass, M is the molar mass of oxygen, R is the gas constant, T is the temperature of gas, which is 25 °C. Besides, P_{in} is calculated using the following Young-Laplace equation:

$$P_{\text{in}} = P_{\text{out}} + \frac{2\gamma}{d/2}, \quad (19)$$

where P_{out} is the pressure outside the bubble, γ is the surface tension of alkaline liquid, which is considered to be almost equal to that of water. Eq. 18 and 19 yield the mass m of the bubble with diameter d . Thus, the diameter distribution (Fig. 4a) is converted to the mass distribution (Fig. 4b).

Here, to divide the mass distribution into three size classes, the size class boundaries X1-X2 and X2-X3 are set at 60 μm and 180 μm , respectively. The representative diameters of X1, X2, and X3 are set to 30, 90, and 270 μm , respectively. These parameters for the class boundaries and the representative diameters were selected to make the discussion simple. Note that selecting the average diameter of a size class, which can be obtained by calculating the average mass of the size class and substituting it into Eq. 18, as its representative diameter was also an option. However, we chose to fix the representative diameters over all the current density conditions in order to make the discussion simple. Hence, for a given size class i , the representative diameter d_i remains constant regardless of current density, while the mass allocation coefficient c_i , calculated as the ratio of the total mass of the size class i to the total mass of all the size classes, varies with the current density. The calculated c_i is summarized in Fig. 5.

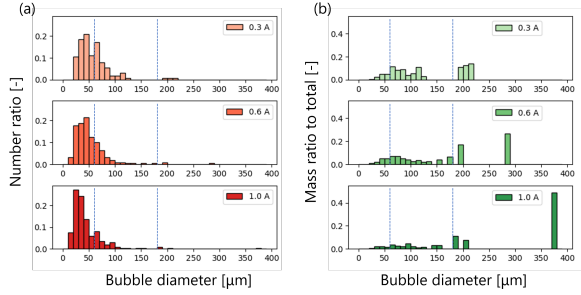


Figure 4: Histograms of (a) bubble diameter distribution and (b) mass ratio to the total mass. The blue dot lines show the size class boundaries: 60 μm for the boundary between X1 and X2, and 180 μm for the boundary between X2 and X3

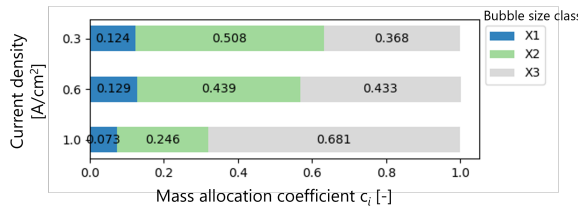


Figure 5: The mass allocation coefficients for size classes at each current density.

6. Results and discussion

In Fig. 6, the transition of the volume fraction field for each phase at 0.6 A/cm² is illustrated. Due to the cell's structure, the liquid phase formed a circulating flow. Size class X1 flowed along the liquid circulation, while X3 flowed directly out into the outlet without circulating, and the flow field of X2 exhibited characteristics of both X1 and X3. This difference is primarily explained by the balance between drag and buoyancy, which are proportional to the square and cubic of the bubble diameter, respectively. The specific surface area of the bubble plays a key role in the flow field. The smaller the bubble, the larger its specific surface area, making it easier to flow along the liquid phase. This trend was similarly observed in the calculations at 0.3 and 1.0 A/cm².

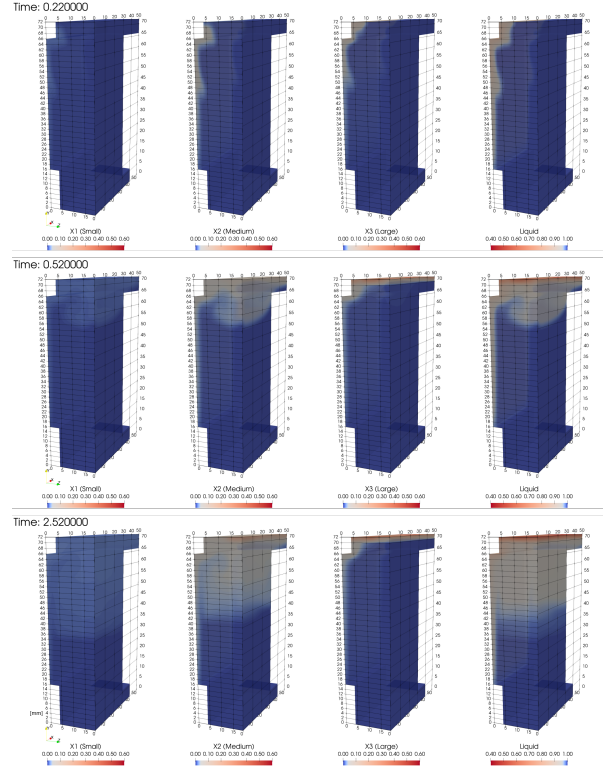


Figure 6: The phase volume fraction fields for each bubble size class and the liquid phase at $t = 0.22, 0.52$, and 2.52 s.

The appreciable difference observed among different current densities was in the height of the bubble circulating flow, which we define as the length measured along y-direction from the top surface of the geometry to the bottom end of the bubble circulating flow. This was compared to the experimental

visualization as shown in Fig. 7 c. The flow inside the cell was visualized from the side during the steady operation at each of three current densities. In a video, the height of the bubble circulating flow fluctuated, which made the comparison complex, so the 20 seconds of it was time-averaged to a single picture and converted into a gray-scale image. On the other hand, as for the simulation figure, to compare it to the experimental visualization, the volume fraction field at each current density was averaged over x -direction from $x = 0$ to $x = 30$ [mm]. In the experiment, the bubble pool volume at the top grew as the current density increased, but in the simulation, the top surface of the geometry was defined to be the same height as the top surface of the outlet hole, which is indicated by the top end of the line A-A' in Fig. 7b and c. The gas volume fractions (GVF) (Fig. 7a) from the simulations, and the brightness values (BV) (Fig. 7d) from the experimental images were obtained as the profiles on the line A-A'. To compare the height of the bubble circulating flow, we focused on the position where the GVF and the BV drop to the minimum values in the range of the solid lines in Fig. 7a and d. Note that comparing the absolute values of the BVs among the different current densities is not simple because the changes in the BV do not always translate linearly into the GVF. Therefore, the absolute values of BV among different current densities are not compared, and accordingly, the scale of each plot is adjusted so that the widths of the purple dash-dot lines in Fig. 7d are consistent across the different current densities. This scale adjustment was also applied to the plots in Fig. 7d. From Fig. 7a and d, the simulation successfully reproduced the increase in the height of the bubble circulating flow. However, as the current density increased, the simulated height of the bubble circulating flow was slightly overestimated compared to the experimental one. We consider this is because the simulation didn't take into account the bubbles trapped into the bubble pool and eventually discharged into the air from the top outlet. This problem can be handled by incorporating bubble coalescence and breakage or assigning appropriate boundary conditions to the top surface.

As explained in Section 1, the advantage of the presented method over CFD-PBM coupled models is that it is easier to simulate flow systems where there are significant differences in velocity fields depending on the different sizes of the dispersed phase. Here, to demonstrate the advantage of the

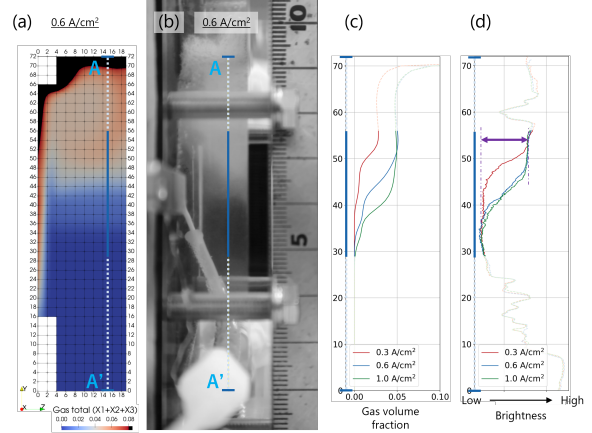


Figure 7: Comparison of simulation results and the experimental visualization: (a) simulated liquid volume fraction field averaged over the electrode width (30mm) at $0.6 \text{ A}/\text{cm}^2$, with the volume fraction above 0.08 excluded from color legend, (b) experimental visualization time-averaged over 20 seconds at $0.6 \text{ A}/\text{cm}^2$, (c) the gas volume fraction profiles on line A-A' of simulations at each current density, and (d) the brightness value profiles on line A-A' from the experimental visualizations at each current density.

presented method, a simulation with only medium size bubble (named simulation “M”) was performed and the liquid volume fraction on the surface of the electrode was compared to that of the simulation with three bubble sizes (named simulation “SML”). Fig. 8 shows the plots of average liquid volume fraction (ALVF) over time in the lower ($y = 20$ to 30 [mm], $z = 0$) and upper ($y = 50$ to 60 [mm], $z = 0$) area selections on the electrode surface. The

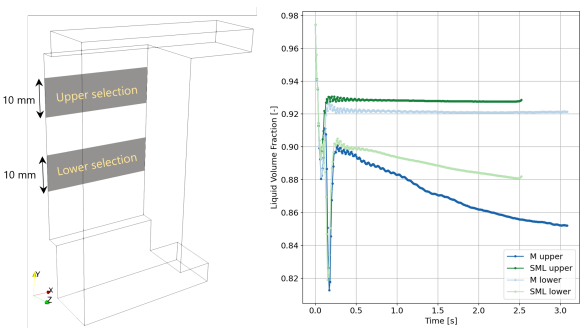


Figure 8: Comparison of the average liquid volume fraction on the two selected areas over time between the simulation with three bubble size classes (“SML”) and that with one bubble size class (“M”) at $1.0 \text{ A}/\text{cm}^2$

ALVFs drop right after bubble generation ($t = 0$ to $t \approx 0.1$ [s]) for both the upper and lower selec-

tions in the two simulations. Subsequently, in the upper selection, the ALVF further decrease owing to rising bubbles from the lower part of the electrode. Eventually, for both the upper and lower selections, the ALVF begin to increase and settle to almost constant values. Overall, simulation “M” underestimates the ALVF compared to simulation “SML”. This comparison suggests the importance of considering multiple sizes for the dispersed phase.

7. Summary

Achieving more precise predictions of bubble flow is crucial for the design of high-performance water electrolyzers. The treatment of dispersed bubble size significantly influences the simulation results. While monodisperse models commonly used for predicting bubble flow in water electrolysis cells often yield inadequate predictions, there is a lack of examples utilizing the polydisperse model, such as the Population Balance Model (PBM), for simulating bubble flow including circulating flow inside water electrolysis cells.

In this study, a new model was proposed that classifies the dispersed gas bubble phase into multiple bubble size classes based on bubble diameter and calculate individual velocity and volume fraction fields for each size class. This model successfully simulated distinct flow fields of each size class, which is attributed to differences in their specific surface areas. The simulation results were validated against experimental visualization for several current densities. Furthermore, using this model, a simulation with multiple size classes and that with a single size class were compared, confirming differences in their bubble volume fractions in the vicinity of the electrode surface.

8. Acknowledgements

This study was based on results obtained from the Development of Fundamental Technology for Advancement of Water Electrolysis Hydrogen Production in Advancement of Hydrogen Technologies and Utilization Project (JPNP20003) commissioned by the New Energy and Industrial Technology Development Organization (NEDO).

References

- [1] I. E. A. (IEA), The future of hydrogen, Tech. rep. (2019).
- [2] J. Brauns, T. Turek, Alkaline water electrolysis powered by renewable energy: A review, *Processes* 8 (2020) 248. doi:10.3390/pr8020248.
- [3] O. Schmidt, A. Gambhir, I. Staffell, A. Hawkes, J. Nelson, S. Few, Future cost and performance of water electrolysis: An expert elicitation study, *International Journal of Hydrogen Energy* 42 (2017) 30470–30492. doi:10.1016/j.ijhydene.2017.10.045.
- [4] A. Buttler, H. Spiethoff, Current status of water electrolysis for energy storage, grid balancing and sector coupling via power-to-gas and power-to-liquids: A review, *Renewable and Sustainable Energy Reviews* 82 (2018) 2440–2454. doi:10.1016/j.rser.2017.09.003.
- [5] A. Angulo, P. van der Linde, H. Gardeniers, M. Modestino, D. F. Rivas, Influence of bubbles on the energy conversion efficiency of electrochemical reactors, *Joule* 4 (2020) 555–579. doi:10.1016/j.joule.2020.01.005.
- [6] S. Park, L. Liu, C. Demirkir, O. van der Heijden, D. Lohse, D. Krug, M. T. M. Koper, Solutal marangoni effect determines bubble dynamics during electrocatalytic hydrogen evolution, *Nature Chemistry* 15 (2023) 1532–1540. doi:10.1038/s41557-023-01294-y.
- [7] M. M. Bakker, D. A. Vermaas, Gas bubble removal in alkaline water electrolysis with utilization of pressure swings, *Electrochimica Acta* 319 (2019) 148–157. doi:10.1016/j.electacta.2019.06.049.
- [8] C. Multiphysics, Modeling and simulation of multiphase flow in comsol multiphysics: Part1.
- [9] R. S. Jupudi, H. Zhang, G. Zappi, R. Bourgeois, Modeling bubble flow and current density distribution in an alkaline electrolysis cell, *The Journal of Computational Multiphase Flows* 1 (2009) 341–347. doi:10.1260/1757-482x.1.4.341.
- [10] M. Dreoni, F. Balduzzi, G. Ferrara, A. Bianchini, Accuracy assessment of the eulerian two-phase model for the cfd simulation of gas bubbles dynamics in alkaline electrolyzers, *Journal of Physics: Conference Series* 2385 (2022) 012040. doi:10.1088/1742-6596/2385/1/012040.
- [11] D. L. Bideau, P. Mandin, M. Benbouzid, M. Kim, M. Sellier, F. Ganci, R. Inguanta, Eulerian two-fluid model of alkaline water electrolysis for hydrogen production, *Energies* 13 (2020) 3394. doi:10.3390/en13133394.
- [12] H. Ikeda, R. Misumi, Y. Kojima, A. A. Haleem, Y. Kuroda, S. Mitsushima, Microscopic high-speed video observation of oxygen bubble generation behavior and effects of anode electrode shape on oer performance in alkaline water electrolysis, *International Journal of Hydrogen Energy* 47 (2022) 11116–11127. doi:10.1016/j.ijhydene.2022.01.166.
- [13] R. Wedin, L. Davoust, A. Cartellier, P. Byrne, Experiments and modelling on electrochemically generated bubbly flows, *Experimental Thermal and Fluid Science* 27 (2003) 685–696. doi:10.1016/s0894-1777(03)00073-6.
- [14] P. Boissonneau, P. Byrne, An experimental investigation of bubble-induced free convection in a small electrochemical cell, *Journal of Applied Electrochemistry* 30 (2000) 767–775. doi:10.1023/A:1004034807331.
- [15] A. Zarghami, N. Deen, A. Vreman, Cfd modeling of multiphase flow in an alkaline water electrolyzer, *Chemical Engineering Science* 227 (2020) 115926. doi:10.1016/j.ces.2020.115926.
- [16] A. Alexiadis, M. Dudukovic, P. Ramachandran, A. Cornell, J. Wanngård, A. Bokkers, Liquid-gas flow patterns in a narrow electrochemical channel,

- Chemical Engineering Science 66 (2011) 2252–2260. doi:10.1016/j.ces.2011.02.046.
- [17] D. Li, Z. Li, Z. Gao, Quadrature-based moment methods for the population balance equation: An algorithm review, Chinese Journal of Chemical Engineering 27 (2019) 483–500. doi:10.1016/j.cjche.2018.11.028.
- [18] P. Chen, J. Sanyal, M. Dudukovic, Cfd modeling of bubble columns flows: implementation of population balance, Chemical Engineering Science 59 (2004) 5201–5207. doi:10.1016/j.ces.2004.07.037.
- [19] M. Bhole, J. Joshi, D. Ramkrishna, Cfd simulation of bubble columns incorporating population balance modeling, Chemical Engineering Science 63 (2008) 2267–2282. doi:10.1016/j.ces.2008.01.013.
- [20] J. Sanyal, D. L. Marchisio, R. O. Fox, K. Dhanasekharan, On the comparison between population balance models for cfd simulation of bubble columns, Industrial & Engineering Chemistry Research 44 (2004) 5063–5072. doi:10.1021/ie049555j.
- [21] Y.-Q. Liu, J.-H. Tay, Cultivation of aerobic granules in a bubble column and an airlift reactor with divided draft tubes at low aeration rate, Biochemical Engineering Journal 34 (2007) 1–7. doi:10.1016/j.bej.2006.11.009.
- [22] OpenCFD, Openfoam: Api guide v2006 reactingmultiphaseeulerfoam.
- [23] Schiller, Links, A drag coefficient correlation, Zeit. Ver. Deutsch. Ing. 77 (1933) 319–320.
- [24] D. Drew, L. Cheng, R. Lahey, The analysis of virtual mass effects in two-phase flow, International Journal of Multiphase Flow 5 (1979) 233–242. doi:10.1016/0301-9322(79)90023-5.
- [25] D. Drew, R. Lahey, The virtual mass and lift force on a sphere in rotating and straining inviscid flow, International Journal of Multiphase Flow 13 (1987) 113–121. doi:10.1016/0301-9322(87)90011-5.
- [26] S. Antal, R. Lahey, J. Flaherty, Analysis of phase distribution in fully developed laminar bubbly two-phase flow, International Journal of Multiphase Flow 17 (1991) 635–652. doi:10.1016/0301-9322(91)90029-3.
- [27] N. Lubchenko, B. Magolan, R. Sugrue, E. Baglietto, A more fundamental wall lubrication force from turbulent dispersion regularization for multiphase cfd applications, International Journal of Multiphase Flow 98 (2018) 36–44. doi:10.1016/j.ijmultiphaseflow.2017.09.003.
- [28] A. D. Burns, T. Frank, I. Hamill, J.-M. Shi, The favre averaged drag model for turbulent dispersion in eulerian multi-phase flows, Vol. 4, 2004, pp. 1–17.
- [29] R. Hreiz, L. Abdelouahed, D. Fünfschilling, F. Lapicque, Electrogenerated bubbles induced convection in narrow vertical cells: Piv measurements and euler-lagrange cfd simulation, Chemical Engineering Science 134 (2015) 138–152. doi:10.1016/j.ces.2015.04.041.
- [30] S. Lee, W. Sutomo, C. Liu, E. Loth, Micro-fabricated electrolytic micro-bubbler, International Journal of Multiphase Flow 31 (2005) 706–722. doi:10.1016/j.ijmultiphaseflow.2005.02.002.